# Heat Balance in the Nordic Seas in a Global 1/12° Coupled Model

ANNE MARIE TREGUIER,[a] PIERRE MATHIOT,[b] TIM GRAHAM,[b] DAN COPSEY,[b] CAMILLE LIQUE,[a] AND JEAN STERLIN[c]

[a] *Univ. Brest, CNRS, IRD, Ifremer, Laboratoire d'Oceanographie Physique et Spatiale, IUEM, Brest, France*
[b] *Met Office, Exeter, United Kingdom*
[c] *Georges Lemaître Centre for Earth and Climate Research, Earth and Life Institute, Université Catholique de Louvain, Louvain-la-Neuve, Belgium*

(Manuscript received 31 January 2020, in final form 25 September 2020)

ABSTRACT: The Nordic seas are a gateway to the Arctic Ocean, where Atlantic water undergoes a strong cooling during its transit. Here we investigate the heat balance of these regions in the high-resolution Met Office Global Coupled Model GC3 with a 1/12° grid. The GC3 model reproduces the contrasted ice conditions and ocean heat loss between the eastern and western regions of the Nordic seas. In the west (Greenland and Iceland seas), the heat loss experienced by the ocean is stronger than the atmospheric heat gain, because of the cooling by ice melt. The latter is a major contribution to the heat loss over the path of the East Greenland Current and west of Svalbard. In the model, surface fluxes balance the convergence of heat in each of the eastern and western regions. The net east–west heat exchange, integrated from Fram Strait to Iceland, is relatively small: the westward heat transport of the Return Atlantic Current over Knipovich Ridge balances the eastward heat transport by the East Icelandic Current. Time fluctuations, including eddies, are a significant contribution to the net heat transports. The eddy flux represents about 20% of the total heat transport in Denmark Strait and across Knipovich Ridge. The coupled ocean–atmosphere–ice model may overestimate the heat imported from the Atlantic and exported to the Arctic by 10% or 15%. This confirms the tendency toward higher northward heat transports as model resolution is refined, which will impact scenarios of future climate.

KEYWORDS: Arctic; Atmosphere-ocean interaction; Ocean dynamics; Eddies; Climate models; Oceanic variability

## 1. Introduction

Situated between the Greenland–Scotland Ridge and Fram Strait, the Nordic seas are the gateway between the North Atlantic and the Arctic (Fig. 1). This region of the World Ocean is of considerable importance because of its role in driving the Atlantic meridional overturning circulation (AMOC). It is established that the overflows over the Greenland–Scotland Ridge and the entrainment just downstream of the sills account for at least two-thirds of the dense branch of the AMOC [12 Sv (1 Sv $\equiv 10^6\,m^3\,s^{-1}$); Quadfasel and Käse 2007], and recent transport measurements confirm that view (Lozier et al. 2019; Chafik and Rossby 2019). These overflows are fed by waters of Arctic and Atlantic origin that have been transformed in the Nordic seas by interior mixing and by exchanges with the atmosphere. Regarding the Arctic watermass transformations, the Nordic seas play a preconditioning role by cooling the warm Atlantic waters before they enter the Arctic Ocean through Fram Strait and the Barents Sea (Moat et al. 2014). The heat transport of these Atlantic waters has a strong impact on Arctic basin properties (Polyakov et al. 2017; Barton et al. 2018) and Arctic climate (Docquier et al. 2019), and it has been demonstrated to be a source of predictability on interannual to decadal time scales in the Nordic seas and Barents Sea in CMIP5 models (Langehaug et al. 2017).

There is a sharp contrast between the Norwegian Sea in the east and the Greenland and Iceland Seas in the west. Water of Atlantic origin circulates in the Norwegian Sea, where the heat loss to the atmosphere is large. The Greenland and Iceland Seas are fed by the cold waters of the East Greenland Current entering through Fram Strait, and they are partly covered by sea ice in winter. The complexity and variability of the ice conditions make it very difficult to quantify air–sea fluxes over the area. Moreover, ice–ocean fluxes that impact water mass properties are not observable directly. Although the entrance and exits of the Nordic seas have been monitored for decades (Dickson et al. 2008), the exchanges between the eastern and western part, across the Arctic front, are not well known. Two eastward flowing currents have been described: the Jan Mayen Current, at the latitude of the Jan Mayen island (Bourke et al. 1992) and the East Icelandic Current, north of Iceland (Jónsson 2007). A westward recirculation branch, the Return Atlantic Current (Bourke et al. 1988), is found at the latitudes of Fram Strait and may be eddy driven (Hattermann et al. 2016). In a pioneering paper, Segtnan et al. (2011) constructed a full heat balance of the Nordic seas from observations. They compared the heat convergence into individual basins with the atmospheric heat loss from reanalyses, and concluded that a significant export of heat from the Norwegian Sea into the Greenland and Iceland Seas was necessary to close the budget. However the observations were not dense enough in space and time to infer the nature (mean flow or eddies) and the location of this heat export. Recently, Asbjørnsen et al. (2019) computed the heat budget in the Norwegian Sea using the ECCOv4 ocean reanalysis. They analyzed the sources of interannual variability,

*Corresponding author*: Anne Marie Treguier, anne-marie.treguier@univ-brest.fr

DOI: 10.1175/JCLI-D-20-0063.1

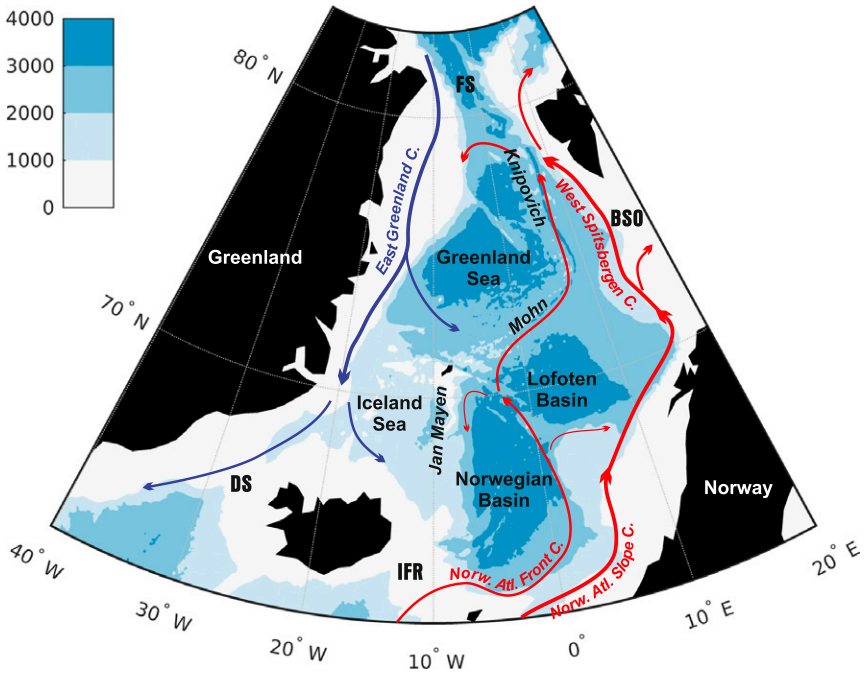


FIG. 1. Bathymetry of the Nordic seas (m). The main straits allowing exchanges with the Atlantic and the Arctic are indicated: Denmark Strait (DS), Iceland Faroe Ridge (IFR), Barents Sea opening (BSO), and Fram Strait (FS), as well as the main seas (Greenland, Iceland, Norwegian Seas), deep ocean ridges (Knipovich, Mohn, and Jan Mayen), and the two deep basins of the Norwegian Sea (Lofoten Basin and Norwegian Basin). The bathymetric field is taken from the GC3 1/12° model. The main currents carrying Atlantic Water are outlined in red (Norwegian Atlantic Slope Current, Norwegian Atlantic Front Current, West Spitzbergen Current). The East Greenland Current, carrying Arctic Water, is outlined in blue. The current paths are based on Taburet et al. (2019).

and concluded that ocean advection was the main driver of heat content variability, the surface fluxes being less important, but their study was limited to the Atlantic water domain south of 75°N.

In this paper, we take advantage of a new global coupled ocean–atmosphere–ice model to study the full depth heat balance of the Nordic seas and the exchanges of heat between the different subbasins. This global model (Hewitt et al. 2016) has an unprecedented fine resolution of 1/12° in the ocean, comparable to the state-of-the-art regional models used to investigate the circulation in the Nordic seas. Previous studies at high resolution have mainly used ocean models forced by an observed atmospheric state, rather than coupled models. A recent example is Ypma et al. (2019), who estimate Atlantic water fluxes through Denmark Strait in two global ocean models at 1/10°. Despite being forced by the same CORE dataset, these models have very contrasted sea ice concentrations in the Nordic seas, and both differ from observations. In such forced models, one may question the validity of air–sea fluxes on account of the mismatch between observed air temperature and modeled sea surface temperature where observed and modeled ice concentrations differ (Griffies et al. 2009). In coupled models in contrast, exchanges between the ocean, ice, and atmosphere are fully consistent, which is an advantage for a study of the heat budget, provided that the coupled model has a stable climate under constant external forcing. This is the case for the GC3 model in our region of interest.

The paper is organized as follows. After a presentation of the model characteristics, the surface properties and mass transports are compared with observations in section 3, and the heat budget of the Nordic seas is presented in section 4. We show how the full-depth convergence of heat is balanced by the exchanges with the atmosphere and sea ice at the surface in the different subbasins of the Nordic seas, we quantify for the first time the east–west exchanges, and we assess the role of eddies in driving the heat transports. Finally, we document the interannnual varibility of the east–west transports within the Nordic seas over the period of the simulation (30 years).

## 2. Model description

The Earth system model used in this study is based on the Met Office Global Coupled 3.0 (GC3) configuration (Williams et al. 2018), incorporating the Global Atmosphere 7 (GA7) and the Global Land 7 (GL7) configurations (Walters et al. 2019), the Global Ocean 6 (GO6) configuration (Storkey et al. 2018), and the Global Sea Ice configuration (Ridley et al. 2018). The atmospheric model has 85 levels on the vertical

and a N512 horizontal grid (15 km over the Nordic seas). The ocean model is based on the NEMO modeling platform in geopotential coordinate with 75 levels (1-m resolution at the surface) on the global tripolar grid eORCA12 (1/12° nominal resolution; i.e., a 4.7-km averaged resolution in the Nordic seas). The sea ice model is based on the version 5.2.1 of the CICE base code (Hunke et al. 2015) setup with five ice thickness categories, four ice layers, and one snow layer. The coupling between the ocean/ice component and the atmosphere component is done with OASIS3-MCT (Craig et al. 2017) at a frequency of 1 h. All the results described here are based on a present-day climate experiment. This is a 50-yr free-running simulation with constant forcing values from year 2000 (solar forcing, aerosols, ozone, and greenhouse gas concentrations). The experiment is initialized as follows. The atmosphere initial state comes from a 1-yr simulation of a GC3 N512-eORCA025 (global ocean at 1/4°) with forcing from year 2000. The ocean temperature and salinity are initialized from a climatology based on the EN4 objective analysis (Good et al. 2013) for the period 1995–2014. This period is long enough to define a climatological state and it includes the year 2000, which has been chosen for the external forcing. The ocean model is spun up from rest. The sea ice initial condition is a snapshot from an eORCA12 G06 simulation forced by atmospheric data.

GC3 is a pre-CMIP6 model version. Extensive validation of the GC3 N512-O012 was not published. A previous version of a Global Coupled configuration (GC2.1) has been evaluated at such resolution in the atmosphere and the ocean by Hewitt et al. (2016). Relative to GC2, the main changes in GC3 are a new aerosol scheme, a new multilayer snow scheme on land, a multilayer sea ice scheme, and several parameterization changes in the cloud, the radiation, and the convection component. For CMIP6, the version GC3.1 has been built starting from GC3.0 with the inclusion of a representation of spectral dispersion in the calculation of the cloud droplet effective radius following Liu et al. (2008), followed by further tuning of the sea ice. The differences between GC3.0 and GC3.1 are relatively small and, except for the Southern Ocean, have localized impact (Williams et al. 2018). A GC3.1 N512/O012 configuration had been assessed and evaluated against the lower-resolution configuration as part of the HighResMIP exercise and results are described in detail in Roberts et al. (2019). In the present study, the last 30 years of the GC3 simulation are used and the model is evaluated in the Nordic seas using atmospheric reanalyses and a climatology of surface currents from drifters (Laurindo et al. 2017), as well as satellite observations of sea surface temperature (Reynolds et al. 2007) and ice concentration from the National Snow and Ice Data Center (NSIDC; Cavalieri et al. 1996).

Besides the model prognostic variables (velocity and tracers), products of temperature and velocity are computed online during the simulation at each time step, averaged monthly, and stored on the native model grid. It is thus possible to compute heat fluxes taking into account the eddy variability at all time scales, by substracting the flux due to the time-mean flow from the total (see section 4c). The calculation of transports and tracer fluxes across sections is performed following staggered model grid lines, for consistency with the discretized volume conservation equation [see Fig. 1 of Deshayes et al. (2014) for an illustration]. The domains in which flux convergence and surface forcings are integrated are bounded by these staggered sections or by land grid points.

## 3. Simulated surface properties and transports

The coupled model evaluation is focused on key aspects relevant to ocean heat transport and heat exchange with the atmosphere. We consider sea surface temperature and ice concentration because of their strong influence on air–sea fluxes. The realism of the volume transports through key sections is also assessed, as a prerequisite to the computation of heat transports.

### *a. Sea ice concentration, temperature, and eddy kinetic energy*

The Greenland and Iceland Seas are characterized by the large extent of their seasonal sea ice. Figure 2 shows the contrast in ice concentration between March and September climatologies of the coupled model. Two isolines of sea ice concentration, 0.15 and 0.85, are outlined in gray for the model and red for the observations. In March, the maximum extent of pack ice (ice concentration $> 0.85$) is well represented by the model along the Greenland coast, but the marginal ice zone (MIZ), with concentrations between 0.15 and 0.85, is too wide. On the contrary, the model underestimates the sea ice in Fram Strait and north of Svalbard (Fig. 2a). In September when the ice is minimum (Fig. 2b), the model ice concentration agrees remarkably well with observations in the Greenland Sea, but it is still underestimated north of Svalbard. Regarding the Greenland Sea, Hewitt et al. (2016) also found an overestimation of sea ice with a pattern similar to Fig. 2 (their Fig. 6), which was worse with the 1/4° ocean compared with the 1/12° version.

For a more quantitative comparison, we show in Fig. 3 the ice area over the region from 45°W to 20°E and from 65° to 80°N. It is the sum, over the region, of the area of each cell multiplied by the fractional concentration for that cell. The interannual variability is large in both models and observations, with standard deviations of $5.6 \times 10^4$ and $8.8 \times 10^4$ km$^2$, respectively, which explains some features of the time mean shown in Fig. 2. When the observed ice concentration is high in winter, a protrusion of the MIZ called the Odden extends over much of the Norwegian Sea. Such was the case for example in 1987 and 1997 (Germe et al. 2011). Observations show that the Odden has declined since the 1990s (Germe et al. 2011), which means that this feature has a small footprint on the 1991–2010 average. The modeled MIZ is too extended compared with the observed one (white and red contours in Fig. 2, left panel) because the model develops an Odden-like feature too often, almost every year. Overall, the coupled model shows a realistic seasonal cycle (Fig. 3), albeit with an amplitude larger than observed, related to the overestimation of the Odden. Considering the trends over the 1985–2015 period, a decline of sea ice is observed (Fig. 3a), especially in the Iceland Sea according to Våge et al. (2018). The model shows interannual variability but no trend (Fig. 3b), which is expected

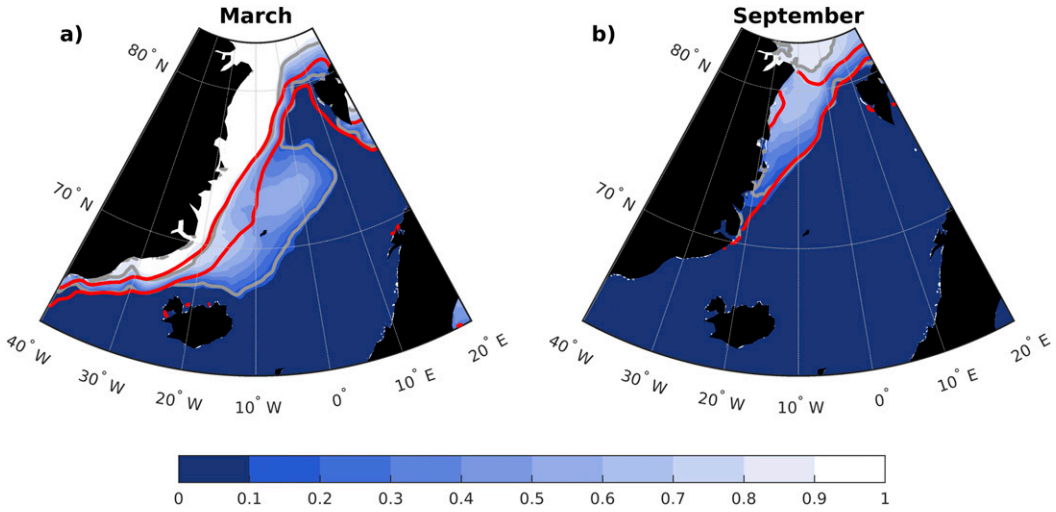


FIG. 2. Ice concentration in the coupled model, averaged over 30 years in (left) March and (right) September. Gray contours indicate ice concentrations of 0.15 and 0.85. The red contours represent concentrations of 0.15 and 0.85 in NSIDC satellite observations for the same months, averaged over the 1991–2010 period.

because the external forcings (anthropogenic and volcanic) are held constant.

The coupled model reproduces the contrasted sea surface temperature distribution of the Nordic seas (Fig. 4a), with warm temperatures along the Norwegian coast and cold temperatures in the Greenland and Iceland seas in the regions partially covered by sea ice. Figure 4b highlights some regions with significant differences between the model and observations. The model SST is slightly too cold in the ice-covered area of the Greenland and Iceland Seas, which is consistent with the large extent of the MIZ in GC3. A cold bias (>2°) is also found in the Lofoten and Norwegian Basins; it seems to be a common feature of the GC2 and GC3.1 coupled simulations analyzed by Hewitt et al. (2016) and Roberts et al. (2019). Wekerle et al. (2017) found a similar bias in the Finite-Element Sea Ice–Ocean Model (FESOM) at 24-km resolution, forced by CORE (their Fig. 4), but in another FESOM simulation at higher resolution (4.5 km), the cold bias was greatly reduced. Such a bias does not appear in the 4-km resolution Regional Ocean Modeling System (ROMS) simulation of Trodahl and Isachsen (2018); note that our SST map in Fig. 4a is directly comparable to their Fig. 2.

Considering that eddies detached from the Norwegian Atlantic Slope Current (NwASC) transport heat into the Lofoten Basin (Isachsen et al. 2012; Dugstad et al. 2019), could the cold bias in GC3 be related to a lack of eddy activity? Figure 5 shows that the eddy energy resulting from the NwASC instabilities is realistic close to the continental slope but underestimated in the western part of the Lofoten Basin, compared to observations by drifters. This eddy energy pattern in CG3 is similar to the ROMS model at 4-km resolution of Isachsen et al. (2012) (their Fig. 4) and Trodahl and Isachsen (2018) (their Fig. 2), as well as to the 4.5-km model of Wekerle et al. (2017) (their Fig. 15), consistent with GC3 having a similar resolution (4.7 km on average in the Nordic seas). Clearly the resolution of GC3 is not yet sufficient to represent the westward drift of eddies into the Lofoten Basin, and their interaction with the Lofoten vortex, a quasi-permanent anticyclonic eddy with a diameter of 18 km (Søiland et al. 2016).

The cold bias in GC3 does not result only from the lack of eddies, but also from an underestimation of the mean advection of warm water by the offshore branch of the Norwegian Atlantic Current, the Norwegian Atlantic Front Current (NwAFC). Repeated observations at the Svinøy section near 63°N have been used to quantify the two branches of the Norwegian Current (Orvik et al. 2001). These authors suggest that the NwAFC transports 3.4 Sv of Atlantic water saltier than 35 psu, an amount similar to the NwASC (4.2 Sv). Mork and

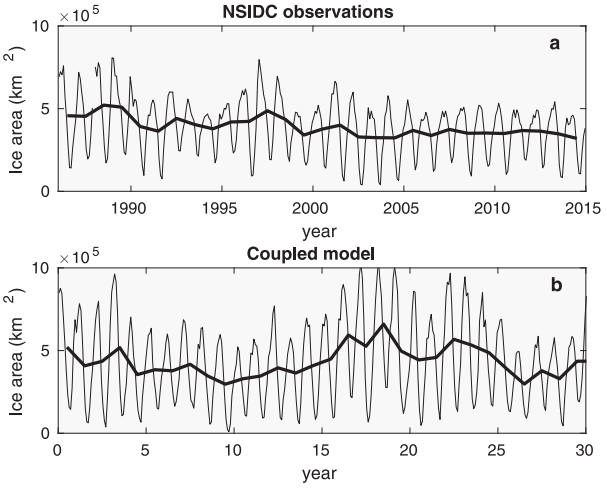


FIG. 3. Ice area in the region 45°W–20°E, 65°–80°N, monthly (thin lines) and annual averages (thick line): (a) observations and (b) coupled model.

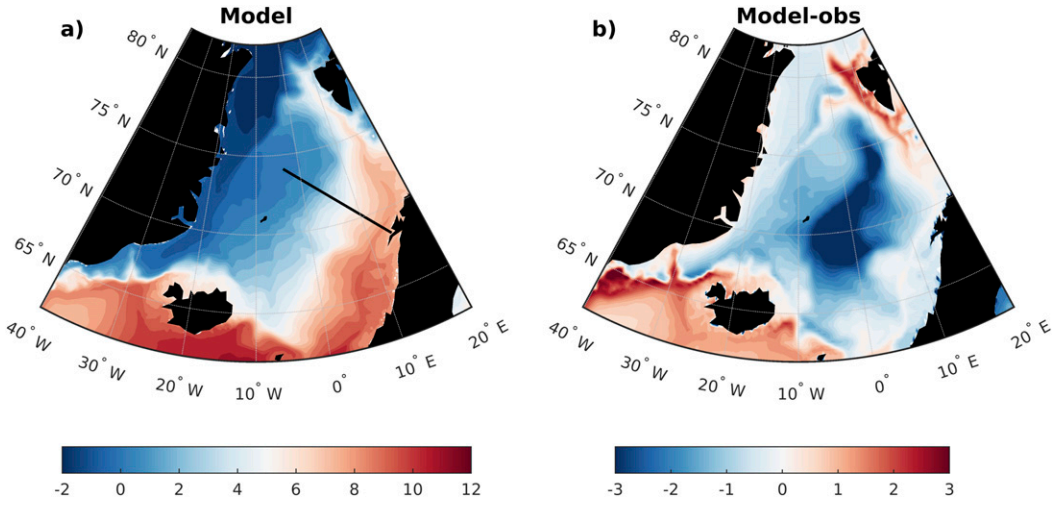


FIG. 4. (a) Sea surface temperature (°C) averaged over 20 years in the coupled model. The black line is the path of the Gimsøy section, used for Fig. 6. (b) Difference between model SST and observed SST (averaged over years 1991–2010).

Skagseth (2010), using altimetry and hydrography, found a much lower transport of Atlantic Water by the NwAFC (1.7 Sv), but on the contrary Høydalsvik et al. (2013) suggest that the front transport is even larger than the slope branch (6.8 Sv). GC3 has a weak offshore NwAFC branch carrying only 1.3 Sv of Atlantic water ($S > 35$ psu) and the NwASC slope branch, inshore of the 1000-m isobath, is much stronger (5 Sv). Despite the lack of agreement between different observational studies, we believe that this weak NwAFC branch is a deficiency of our model, with consequenses on the properties in the Lofoten Basin farther north. Figure 6 compares the temperature in the model and in the climatology for the month of June, along the Gimsøy section (which is outlined on the map of SST; Fig. 4a). A clear temperature front is observed across Mohn Ridge (Fig. 6b), similar to synoptic plots of the section (see Gascard and Mork 2008, their Fig. 6.2). This front is the signature of the warm NwAFC flowing northward on the eastern flank of the ridge (Fig. 1). In the GC3 model (Fig. 6a), the front is replaced by a weaker gradient from Mohn Ridge to Norway, hence the waters colder than observed at the surface (Fig. 4b) and also at depth. This underestimation of the NwAFC in the model may be due to a combination of numerical schemes and the representation of bathymetry, both of which have been shown to affect mean current pathways (Barnier et al. 2006). The topographic constraint may be too large in GC3, compared with other models such as FESOM (Wekerle et al. 2017) or ROMS (Trodahl and Isachsen 2018), and force both branches of the

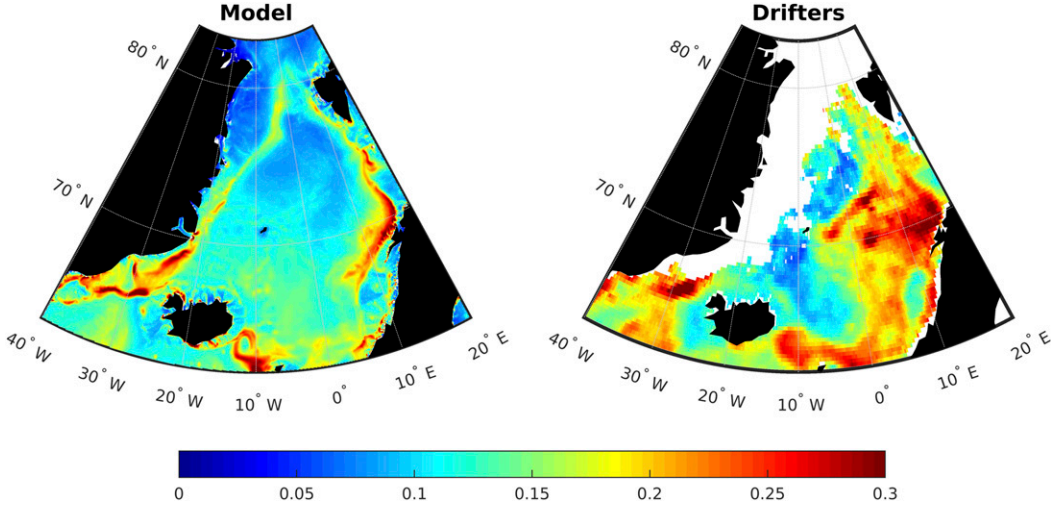


FIG. 5. (left) Root-mean-square (rms) surface velocity ($m\,s^{-1}$) from the GC3 coupled model; (right) rms surface velocity from a climatology of surface drifters (Laurindo et al. 2017).

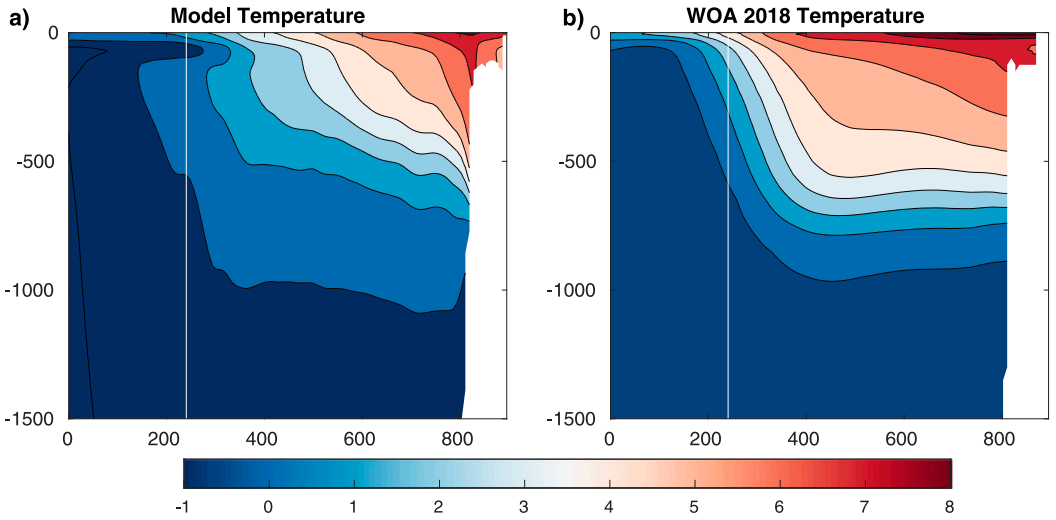


FIG. 6. Climatological temperature (°C) for the month of June along the Gimsøy section, indicated on the map in Fig. 4a. (a) GC3 model monthly mean, averaged over 30 years. (b) Monthly climatology from observations, *World Ocean Atlas 2018* (Locarnini et al. 2018). The white line indicates the top of Mohn Ridge.

Norwegian Atlantic Current to merge to a large extent and to follow the slope.

### b. *Barotropic transports*

To examine further the contrast between the eastern and western parts of the Nordic seas, we have computed the transports into these regions as well as the exchanges between them. The eastern and western regions are delimited by sections following the bathymetric features that separate the deep basins, as in Segtnan et al. (2011). In the western region we have added an additional section between Greenland and the island of Jan Mayen, so that the Greenland and Iceland seas can also be considered separately for some diagnostics. The sections are outlined in Fig. 7 as well as the time-mean barotropic transport through each of them (red numbers and arrows). The section at Fram Strait follows the 79°N latitude, and the boundary between the western and eastern part of this section corresponds to the maximum southward barotropic transport cumulated from Greenland.

Let us consider the eastern region. In the Norwegian Sea, the water enters from the Atlantic Ocean over the sills and from the Greenland and Iceland Seas in the west, and exits to the Barents Sea and to the Arctic via Fram Strait, with also a recirculation to the Greenland Sea above Knipovich Ridge. Regarding the sills, 3.9 Sv of light water cross the Iceland Faroe Ridge in the model, within the uncertainty of Rossby et al.'s (2018) estimate (4.46 ± 0.7 Sv). This flow being the origin of the NwAFC, the weakness of this current branch in the model is thus not a source problem but rather related to processes inside the Norwegian Sea as mentioned in section 3a. The light water flux between the Faroe Islands and Norway (3.2 Sv) is in agreement with the long-term measurements of Sherwin et al. (2008) and the synthesis of Chafik and Rossby (2019). The dense overflow in Faroe Bank channel (3.1 Sv) is higher than the estimate of 2.2 Sv by Chafik and Rossby (2019), but the total amount of dense water outflow east of Iceland in the model is closer to the observations (2.6 Sv; Østerhus et al. 2019). Moving north along the Atlantic Water path, one notes that the model transport into the Barents Sea is large (3.1 Sv) compared with the 2 Sv estimated by Smedsrud et al. (2010), but the outflow by the Spitzbergen Current in Fram Strait is

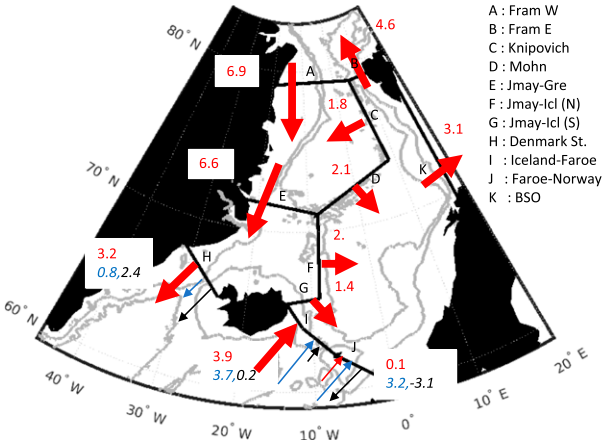


FIG. 7. Mass balance of the Nordic seas in the coupled model. Red arrows (red numbers) represent the depth-integrated ocean mass flux (Sv) across the sections outlined in black. Short names are indicated for the sections; they are used in the tables and explained in the text (e.g., "BSO" for Barents Sea opening). For the southern sections, the two additional numbers (blue and black) indicate the transport associated with mean densities lower and higher than $\sigma_0 = 27.8$, respectively. The sign convention is such that a positive number is a contribution in the same direction as the total indicated by the red arrow. Thin blue and black arrows indicate the direction of these light inflows and dense overflows. The gray contours represent the 500- and 2000-m isobaths.

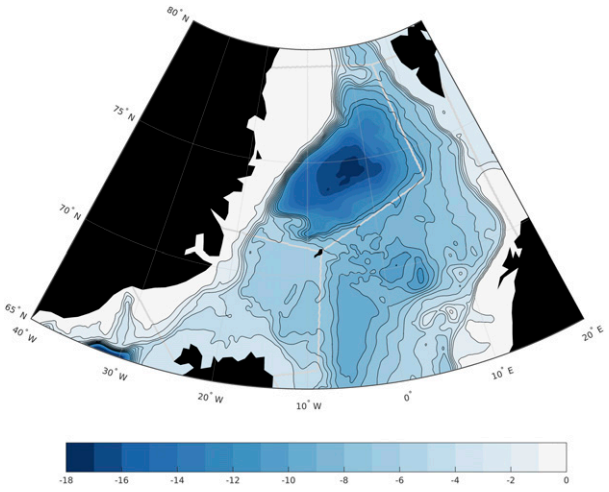


FIG. 8. Barotropic streamfunction (Sv) in the coupled model, averaged over 30 years. The sections delimiting the regions of Fig. 7 are indicated in gray. Only the contours from −1 to −11 Sv are outlined in black, to better show the transports entering and exiting the Greenland gyre, while keeping the readability of the figure.

consistent with observations (Beszczynska-Möller et al. 2012). The Return Atlantic Current, south of Fram Strait, carries 1.8 Sv into the Greenland Sea. This recirculation has been referred to as the Knipovich branch by Aksenov et al. (2010), who computed a transport of 1.2 Sv in their numerical model. de Steur et al. (2014) inferred from currentmeter arrays a recirculation of 3 Sv within 10′ latitude south of 79°N. Based on a synoptic acoustic current meter survey of the EGC, Håvik et al. (2017) find that the Return Atlantic Current contributes 1.6 Sv to the EGC. Overall, the amplitude of this circulation in GC3, 1.8 Sv, seems thus fairly realistic.

Let us consider now the western region (Greenland and Iceland Seas). The East Greenland Current (EGC) carries water through Fram Strait southward, at the rate of 6.9 Sv. Probably because of its high resolution, GC3 has a stronger exchange flow through Fram Strait than the ocean-ice components of climate models analyzed by Ilicak et al. (2016), and more comparable with the inverse estimate of 5.85 Sv by Tsubouchi et al. (2012). The transport entering the Nordic seas through Fram Strait in the coupled model is in very good agreement with the observations reported by Beszczynska-Möller et al. (2012). Marnela et al. (2016) recently obtained a higher transport (11 ± 3 Sv) by summing together all the observed southward flow branches through Fram Strait. The model equivalent is 9.5 Sv, within the range of uncertainty of Marnela et al. (2016).

Mohn Ridge act as a barrier for most of the eastward transport of the Greenland Sea Gyre: the export of 2.1 Sv across this ridge is relatively small, compared with the total transport of the gyre (see Fig. 8 and the discussion hereafter). In the Greenland Sea, more water (2.1 Sv) is exported across Mohn Ridge than the amount imported across Knipovich Ridge (1.8 Sv). This unbalance in water export between the two ridges results in a decrease in the total mass transport along Greenland of 0.3 Sv, between the latitudes of Fram Strait and the island of Jan Mayen. Moving southward into the Iceland Sea, a transport of 6.6 Sv enters between Greenland and Jan Mayen; half of it exits to the North Atlantic through Denmark Strait (3.2 Sv) and half to the Norwegian Sea (3.4 Sv). This latter transport, between Iceland and Jan Mayen, is difficult to validate from observations. The model seems coherent with the circulation diagram of Jónsson (2007), who measure 2.5 Sv in the East Icelandic Current; note that their section does not capture all the eastward flow north of Iceland.

The total barotropic transport through Denmark Strait is also difficult to validate from observations because of the lack of transport measurements over the continental shelf. Østerhus et al. (2019) estimate a net transport of 4.3 Sv, higher than the transport of 3.2 Sv in GC3. This net transport is the result of the exchanges of light and dense waters above the Greenland–Scotland sills, which are the main driver of the AMOC. To compare these inflows and outflows with observations, we have computed the transport for densities above and below $\sigma_0$ = 27.8 (blue and black numbers and arrows in Fig. 7). The overflow of dense water in Denmark Strait, 2.4 Sv in GC3, is indeed lower than observed. Jochumsen et al. (2012), Harden et al. (2016), and Østerhus et al. (2019) estimate it at 3.4, 3.54, and 3.2 Sv, respectively. Averaged across the strait, the light water flows to the south (0.8 Sv), but this net transport is the sum of a southward flow along Greenland and a northward flow along Iceland. The northward flow of Atlantic water is 1 Sv, in agreement with the observed transport of the North Icelandic Irminger Current (Østerhus et al. 2019).

As a result of mass conservation in the model, the net balances in the east and west regions are very small compared to the transports through sections shown in Fig. 7. In the western region (Greenland and Iceland Seas) there is a divergence of −0.055 Sv. Most of this liquid water export is caused by sea ice melt. Indeed, sea ice is advected into the region through Fram Strait, and only partially exported through Denmark Strait, providing a net volume convergence of 0.035 Sv. More precisely, the ice convergence in the western region results from the ice inflow at Fram [0.053 Sv, or 1672 $km^3\,yr^{-1}$, consistent with the recent estimate of Ricker et al. (2018)], which is not compensated by the smaller ice export through Denmark Strait (0.017 Sv; 534 $km^3\,yr^{-1}$). The ice exchange between the western and eastern regions is negligeable, one order of magnitude smaller (0.001 Sv). After taking into account the ice melt, the remaining volume divergence is 0.02 and 0.016 Sv in the western and eastern regions, respectively; it is forced by the input of water due to the precipitation–evaporation balance and the river runoff.

The transport of the Greenland Sea gyre does not appear in Fig. 7 because the gyre lies entirely within the boundaries of the Greenland Sea region (Fig. 8). This gyre is quite strong in the coupled model, with a maximum barotropic streamfunction of 17.6 Sv at its center (computed by integrating the meridional transports eastward from Greenland). In Fig. 8, streamfunction values from −1 to −11 are contoured in black, to show the location of the barotropic exchanges between the Greenland–Iceland and Norwegian Seas in relation with the subregion boundaries, and thus provide a detailed information that

complements Fig. 7. Inside the Greenland Sea gyre, the Knipovich and Mohn Ridge sections as defined do not coincide exactly with a streamfunction contour, hence a local recirculation of about 2 Sv across them. However, the main fluxes exchanged between the Greenland and the Norwegian Seas across these two ridges are clearly located north of Knipovich Ridge (the Return Atlantic Current branch) and at the southern tip of Mohn Ridge, north of Jan Mayen. The flow between Jan Mayen and Iceland is concentrated in the southern part of the Iceland sea, in the East Icelandic Current.

Figure 7 provides a synthetic view of the full-depth water transports at the entrance and exit of the Nordic seas that, to our knowledge, has never been derived from a model analysis. Indeed, most modeling studies focus on specific water masses or straits, for example the Atlantic Water (Aksenov et al. 2010), the water exchange across Denmark Strait (Ypma et al. 2019), or the transports into the Arctic through Fram Strait and the Barents Sea opening (van der Linden et al. 2019). The quantification of the exchange between the Iceland and the Norwegian Seas is also new; only the East Icelandic Current has been observed (Jónsson 2007) but not the flow over the Jan Mayen Ridge. In the next section, we consider the heat transports associated with these volume transports and their role in the heat balance of the Nordic seas.

## 4. Heat balance of the Nordic seas

### a. *Surface ocean cooling in reanalyses and in the coupled model*

In theory, heat fluxes at the ocean surface give us valuable information on the processes that govern the cooling and densification of surface waters in the Nordic seas. Unfortunately, these fluxes are not easy to infer from observations, and one must turn to atmospheric reanalyses. Segtnan et al. (2011) used surface fluxes from two reanalysis products, ERA-40 and NCEP2 for their study of the Nordic seas heat balance. They found that the total heat loss for the 1990–99 period over the Nordic seas (excluding the Barents Sea) was 126 TW in ERA-40 and 10% higher in NCEP2. Here we take advantage of the ERA5 reanalysis at higher resolution to map the spatial and seasonal variability of surface fluxes, and compare it with the air–sea flux computed by the coupled model. In both reanalyses and model, the net atmospheric heat flux is the sum of the shortwave and longwave radiative fluxes, the sensible and latent heat fluxes. Fluxes are computed using bulk formulas and albedos that are different over ocean and ice. The net heat fluxes over partially covered grid cells are a combination of both, weighted by the ice concentration [for more details about CG3, see Hewitt et al. (2011)].

Figures 9a and 9b display the surface heat flux for the months of March and September, and Table 1 presents the fluxes integrated over the western and eastern parts of the Nordic seas [regions defined by Segtnan et al. (2011) and outlined in Fig. 7]. Ice concentration has its extrema in March and September, but not the heat flux; for this reason the annual mean heat flux is not always comprised between the March and September values. The cooling (atmospheric heat gain) in ERA5 for the decade 2001–10 is 132 TW. It occurs mainly in the eastern part of the Nordic seas [about 2/3 in the east and 1/3 in the west, very similar to Segtnan et al. (2011)]. The annual cycle is strong; the cooling in March is about twice the annual mean (note the two different color scales for March and September in Fig. 9). In the east, the cooling extends from the Norwegian coast well into the Norwegian Sea, and is the strongest along Svalbard. In the western part of the Nordic seas, the cooling occurs mainly along the path of the EGC, along the continental slope. In winter, this cooling region is located in the marginal sea ice zone. In September it occurs at the same location, although the ice boundary has moved north. Therefore it appears that this flux is related to the advection by the EGC, more than to the vicinity of the sea ice edge.

The surface flux from ERA5 is the exchange of heat with the ocean or sea ice at the base of the atmosphere, that can be compared with the surface flux computed in the atmospheric component of GC3 (Figs. 9b,c). Overall, the agreement is quite good. The heat loss in the center of the Norwegian Sea is underestimated in the model, which is certainly related to the cold bias (Fig. 4). This confirms that the cold SST in the Norwegian Sea results from a bias in the ocean circulation rather than an excessive atmospheric cooling.

With the coupled model we can estimate directly the heat flux at the ocean surface, below the sea ice (Figs. 9e,f). The ocean experiences a strong heat loss along the path of the EGC. In fact, the ocean surface cooling integrated in the western region is stronger (more negative) than the warming experienced by the atmosphere (Table 1). This difference between the ocean and atmosphere surface fluxes in the coupled model must be due, in part, to ice melting. There is a net ice melt in the Greenland Sea in the annual average, because the advection of ice from the Arctic is larger than the ice export through Denmark Strait, as mentioned in the previous section (a convergence of 0.035 Sv, corresponding to a cooling of 10.6 Tw). The cooling due to ice melt is also in part responsible for the strong heat loss just north of Fram Strait off Svalbard in the model (Figs. 9e,f), larger than suggested by ERA5. The model heat loss may be overestimated in this region; this could be related to the high sea surface temperature of the water flowing along Svalbard and entering the Arctic as shown in Fig. 4. A complete analysis of the difference between the heat fluxes seen by the ocean and by the atmosphere would require all the components of the sea ice heat budget, but some terms are not available in the model output files.

### b. *Full-depth heat convergence in the coupled model*

We compute in the ocean model the total convergence of heat into the two regions, as well as the contributions of mean flow and time fluctuations to this convergence (Table 2). The convergence of heat in the western and eastern region is consistent with the surface heat fluxes, although a residual of 5 TW indicates a warming trend in the Nordic seas in the model, over the 30 years considered. This trend is concentrated in the Norwegian Sea (an equivalent surface flux of 3.7 $W\,m^{-2}$). As the coupled simulation used constant anthropogenic forcings corresponding to the year 2000, it is difficult to conclude whether this trend is a decadal variability simulated by the model or a drift resulting from imperfect model numerics and

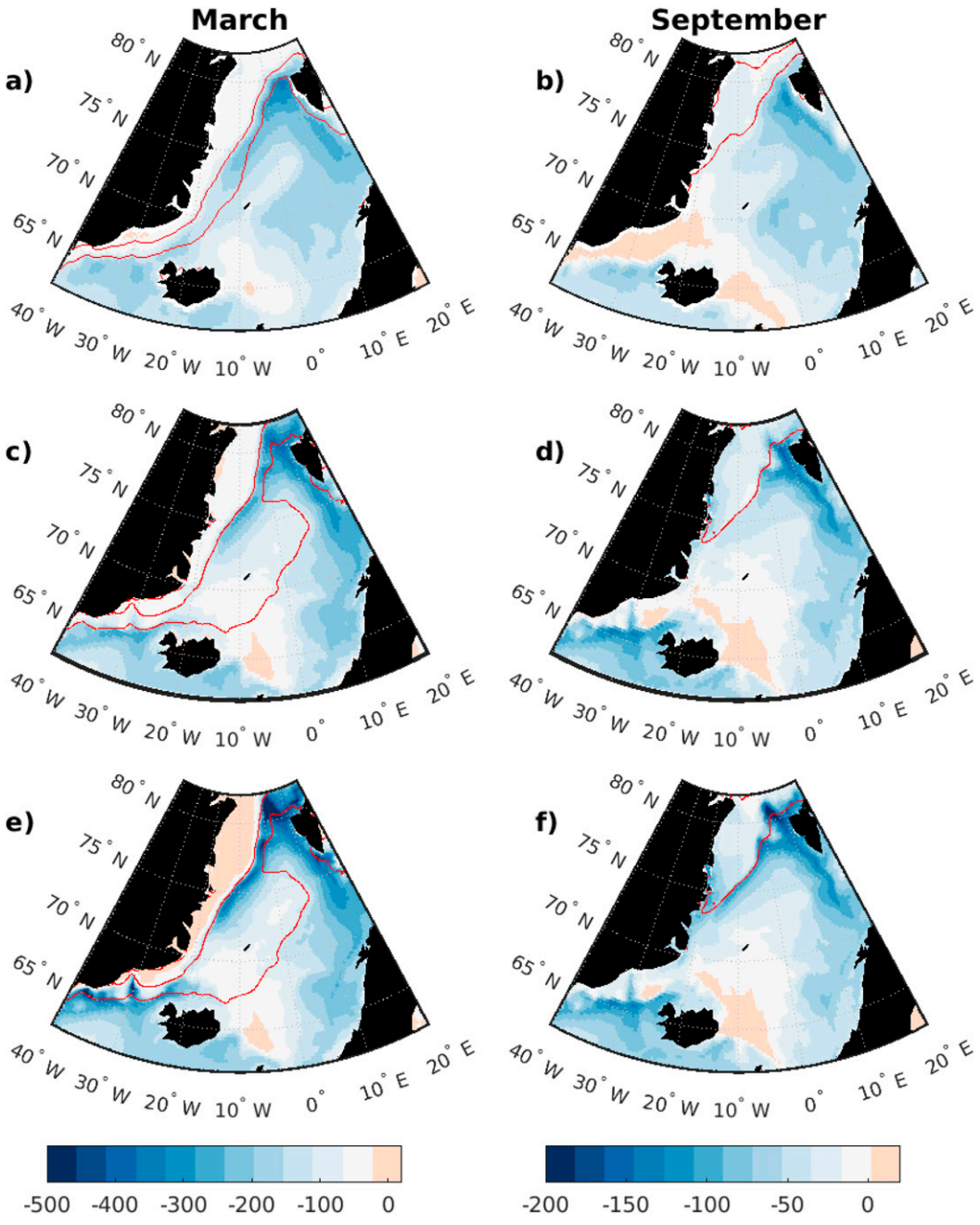


FIG. 9. Surface heat flux climatologies ($W\,m^{-2}$) for (left) March and (right) September, with the limits of the marginal sea ice zone (MIZ) overlaid in red (concentration 0.15 and 0.85). (a),(b) Heat flux at the atmospheric lower boundary from ERA5 (averaged over years 2001–10) and sea ice from NSIDC data. (c),(d) Heat flux at the atmospheric model lower boundary, with the modeled MIZ overlaid. (e),(f) Ocean surface heat flux and modeled MIZ. Note the different color scales for March and September.

parameterizations, or whether it results from a discrepancy between the coupled model forcing and its initial conditions. Observations in the Norwegian basin between 2011 and 2018 (Mork et al. 2019) show a warming of 0.046°C per year in the upper 1000 m, corresponding to a surface flux of 6.3 $W\,m^{-2}$, due to the combination of anthropogenic warming and internal variability. Broomé et al. (2020), using ocean heat content over the Atlantic Water area in the Norwegian Sea, find a warming equivalent to 5 $W\,m^{-2}$ over the period 1993–2002 but no warming between 2004 and 2013. The heat imbalance in the coupled model is thus of a magnitude that does not exceed observed decadal trends and it is not

TABLE 1. Surface heat flux (TW) integrated over the western and eastern parts of the Nordic seas (a negative value represents ocean cooling).

| | Western region | | | Eastern region | | |
|---|---|---|---|---|---|---|
| | Annual mean | March | September | Annual mean | March | September |
| ERA5 surface flux (1991–2010) | −39 | −111 | −24 | −93 | −188 | −61 |
| Atmosphere model surface flux | −27 | −94 | −30 | −90 | −198 | −61 |
| Ocean model surface flux | −47 | −110 | −42 | −96 | −206 | −61 |

larger than drifts and trends found in forced ocean model simulations.

Besides the heat convergence, Table 2 also lists the heat transports across individual sections. The mass transport being nonzero, these numbers depend on the reference temperature. We have chosen 0°C, as in Segtnan et al. (2011) and in almost all estimates from observations (e.g., Østerhus et al. 2005). A regional picture of the full-depth heat balance is provided in Fig. 10. Almost 300 TW of heat enters the Nordic seas over the sills between Greenland and Norway. About half of it is lost to the atmosphere or sea ice (Table 1), and the other half enters the Arctic through the Barents Sea and the Spitzbergen Current. Considering the Norwegian Sea only, 261 TW of heat enters over the Iceland–Scotland Ridge, and the ratio of heat loss processes is about 2/3 of Arctic export and only 1/3 of atmospheric loss. In addition to the exchanges with the Atlantic and Arctic Oceans, Fig. 10 displays the east–west fluxes inside the Nordic seas, and quantifies them in an integrated perspective. The model shows 24 TW of heat entering the Greenland Sea over the Knipovich and Mohn Ridges, contributing to balance the surface heat loss over the Greenland Sea, which is 30.3 TW. In the southern part of the domain, a similar amount of heat (26 TW) is exported from the Iceland Sea into the Norwegian Sea. This export is necessary because the surface heat loss over the Iceland Sea (16.5 TW) does not balance the heat input through Denmark Strait. Integrated from Fram Strait all the way to Iceland, the sum of the east–west exchanges is relatively small (2 TW). Thus, the model gives a consistent picture of the heat balance in the Norwegian Sea with almost no net heat export to the Greenland and Iceland Seas, the exchanges with these two seas compensating each other.

This constrasts with Segtnan et al. (2011), who attempted to construct the heat balance of the western and eastern part of the Nordic seas by estimating the convergence of heat from observations. They found that the total heat convergence in the eastern region (Norwegian Sea), 119 TW, was higher than the surface heat loss by 35 TW, but that the heat convergence in the western region was lower than the surface heat loss by about 36 TW. They concluded that a heat flux from the Norwegian Sea into the Greenland and Iceland Seas was probably necessary to close the heat budget, but they could not

TABLE 2. Heat transport convergence (TW) for the western and eastern parts of the Nordic seas in the GC3 model (a negative value represents ocean cooling). Model transports are averaged over 30 years. The total convergence is the sum of the convergence due to the time-mean flow and the convergence resulting from the time fluctuations (''Transient''). This contribution is further decomposed into a seasonal part and an ''eddy'' part. The heat transports through the sections outlined in Fig. 6 are also listed; the limit between the east and west sections in Fram Strait is the location of the maximum barotropic transport cumulated from Greenland. The sign convention is the following: for the eastern region, all heat transport contributions are counted positive into the region. For the budget of the western region, heat transports at Fram Strait and Denmark strait are positive into the region. The heat transports over Knipovich Ridge and from Mohn Ridge to Jan Mayen and Iceland must be counted with the opposite sign. The heat transport through Fram Strait and the Barent Sea opening are thus shown as negative, representing northward and eastward heat transports into the Arctic.

| Extent | Total | Mean | Transient | Seasonal | Eddy |
|---|---|---|---|---|---|
| | | Heat convergence (TW) | | | |
| Greenland Sea | 30.5 | 25.7 | 4.9 | 0.6 | 4.3 |
| Iceland Sea | 16. | 10.3 | 5.7 | −0.6 | 6.3 |
| Western region | 46.6 | 36 | 10.6 | −0.1 | 10.7 |
| Eastern region | 99.8 | 103.6 | −3.8 | −2.1 | −1.7 |
| | | Heat transport (TW) | | | |
| Fram Strait West | 10.9 | 12.1 | −1.2 | −0.3 | −0.9 |
| Fram Strait East | −70.3 | −69 | −1.3 | 0.5 | −1.8 |
| Denmark Strait (DS) | 37.7 | 29.3 | 8.4 | 0.7 | 7.7 |
| Knipovich Ridge | −22.4 | −17.5 | −4.9 | 0.8 | 4.1 |
| Mohn Ridge | −2.2 | −1.9 | −0.34 | 0.02 | −0.36 |
| Jan Mayen to Iceland | 26.6 | 24.7 | 1.9 | 1.2 | 0.7 |
| Barents Sea opening | −94 | −85.6 | −8.6 | 2.7 | 5.9 |
| Iceland–Faroe (IFR) | 146 | 139 | 8.1 | 0. | 8.1 |
| Faroe–Norway (FSN) | 115 | 113 | 1.4 | −0.3 | 1.7 |

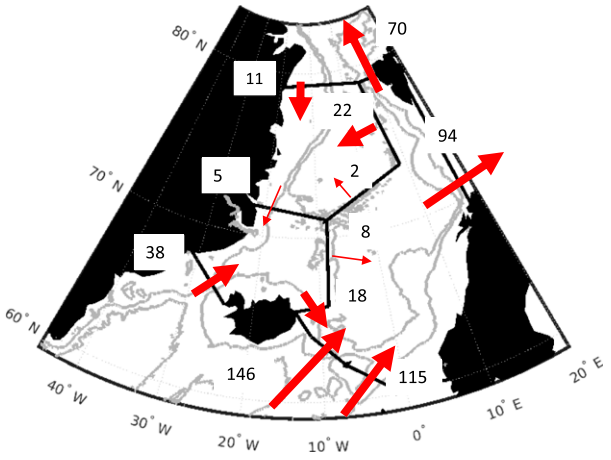


FIG. 10. Heat balance of the Nordic seas in the coupled model. Red arrows represent the heat flux referenced to 0°C (TW) across the sections outlined in black. Values have been rounded relative to the numbers in Table 2 for readability. In the Greenland Sea and in the Iceland Sea the total convergence of heat, 30 and 16 TW, respectively, balances the cooling at the ocean surface within less than 1 TW. In the Norwegian Sea, the heat convergence of 99 TW differs from the surface heat loss (94 TW), generating a warming of 5 TW. The gray contours represent the 500- and 2000-m isobaths.

estimate this exchange due to a lack of data. The difficulty to build a heat balance from observations stems from the fact that most in situ measurements focus on an individual water mass, for example the so-called Atlantic Water (AW). Studies based on these observations use definitions of this water mass that differ from one section to the next, making it impossible to infer robust regional balances from the published literature. We emphasize that in a numerical model, full-depth heat transport calculations such as displayed in Fig. 10 seem the best way to present a consistent heat budget of the Nordic seas.

Is the budget realistic in the coupled model? Model–observation comparisons can be made by calculating a model proxy for the observations; note that in the following, the model transports are not the full-depth values of Table 2 but rather AW transports, each computed with the same method as in the observational reference cited. Three branches of AW entering the Nordic seas have been monitored (Østerhus et al. 2005). The model–data agreement is excellent for the Shetland branch: 112 TW in GC3 versus 107 TW in Berx et al. (2013). The AW model transport in the Faroe branch, measured along a section north of the Faroes, is high: 151 TW in GC3 versus 124 ± 15 TW computed by Hansen et al. (2015). Finally, the Iceland branch in Denmark Strait seems also overestimated in the model: 33 TW in GC3 versus 24 TW in Jónsson and Valdimarsson (2012). Thus, there may be an excess of heat entering the Nordic seas in GC3: the full-depth heat transport from Greenland to Norway, 299 TW, is indeed larger than the 273 Tw estimated by Chafik and Rossby (2019). The excess of heat in the model is not released to the atmosphere and seems to result in larger than observed outflows to the Arctic. Both exit routes have stronger heat transport than observed: the Barents Sea opening with 91 TW versus 70 TW in Smedsrud et al. (2013), as well as Fram Strait with 59 TW in GC3 versus 40 TW in Schauer et al. (2008). This large heat transport from the Atlantic to the Arctic may be related to the high resolution of GC3. Indeed in the CORE model intercomparison Ilicak et al. (2016) found that the model with the highest resolution had the highest heat transports, a finding supported by the comparison of CMIP5 models by Heuzé and Årthun (2019).

Let us add a note of caution regarding the east–west heat exchange in the model. If one considers the volume fluxes west of Fram Strait (6.9 Sv; Fig. 7) and at Denmark Strait (3.2 Sv) as reasonable, this means that a compensating eastward volume flux of about 3.7 Sv exists between Fram Strait and Iceland. In the model the total transport of the eastward flowing branches is even higher (5.5 Sv), to compensate for the westward RAC (−1.8 Sv). The latitudinal distribution of these eastward currents may be affected by the model's weak NwAFC along Mohn Ridge. For example, the 2.1 Sv crossing Mohn Ridge in Fig. 7 could be overestimated and the flow between Jan Mayen and Iceland correspondingly underestimated. Furthermore, the east–west volume transport being nonzero, the associated heat transports depend on the temperature reference. The heat transport across Mohn Ridge in Fig. 10 is opposite to the volume transport because there are negative temperatures over the ridge; it would change sign if the freezing temperature of seawater had been chosen as a reference instead of zero.

### c. *Eddy and seasonal contribution to the time-mean heat fluxes*

The coupled model gives us access to the heat transports due to temporal fluctuations, that is, the correlations of velocity and temperature that can result in a time-mean transport. Let us define $v$ as the velocity normal to a section, $T$ the temperature, the time average by an overbar, and the departures from the time average by primes, and integrate over depth and the length of a section $s$:

$$\iint_s \overline{vT} = \iint_s \overline{v}\,\overline{T} + \iint_s \overline{v'T'}. \quad (1)$$

The $\overline{v'T'}$ correlations occur at all time scales. Table 2 presents separately the heat transport by the time-mean flow and the transients, the latter being further decomposed into a seasonal and an eddy part. The transient seasonal contribution is defined as the difference between the averaged heat transport of 12 monthly means (the monthly climatology being computed over 30 years) and the heat transport by the 30-yr time-mean flow. Overall, the seasonal contribution is smaller than the eddy one. This means that the correlation of the velocity and temperature on seasonal cycles do not contribute much to the total heat transport, despite the large seasonal variability across most sections. For example, the model reproduces the amplification of the recirculation over Knipovich Ridge in winter and spring by a factor of 2 (Hattermann et al. 2016), and the large seasonal cycle of the Atlantic water transport by the Spitzbergen Current in Fram Strait [also a factor of 2 between summer and winter, in agreement with Beszczynska-Möller et al. (2012)].

Let us consider now the transient eddy heat flux. The eddy heat convergence (Table 2) is remarkably large in the Greenland and Iceland Seas, where it represents 23% of the total heat

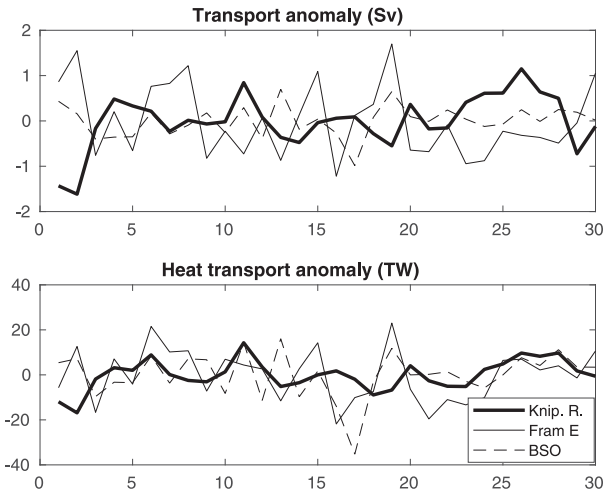


FIG. 11. Interannual anomalies of volume and heat transport across the three sections where warm water exits the Norwegian Sea: Barents Sea opening (BSO), the eastern part of Fram Strait (Fram E), and flow over Knipovich Ridge (Knip. R). All transports are counted positively in the sense of an exit from the Norwegian Sea. The time axis is in model years.

convergence (10.7 TW). It is much smaller in proportion in the Norwegian Sea, 2% of the total. There are two hotspots of eddy heat transport into the Greenland and Iceland Seas (Table 2). One is over Knipovich Ridge, with an eddy flux of 4.1 TW, more than 18% of the total. The second is across Denmark Strait, with an eddy contribution of 7.7 TW representing 20% of the total transport. These strong eddy fluxes are plausible, because the presence of eddies has been documented in the recirculation south of Fram Strait (Hattermann et al. 2016) as well as in Denmark Strait (Appen et al. 2017). The eddy heat fluxes across the Iceland–Faroe Ridge and the Barents Sea opening are also large in magnitude (8.1 and 5.9 TW, respectively) but they represent a lower proportion of the total heat transport,which is large through these sections (146 and 94 TW respectively).

## 5. Interannual variability of heat exchanges between the Greenland–Iceland and Norwegian Seas

Understanding the variability of heat transport from the North Atlantic into the Arctic is crucial in the context of Arctic climate change. This variability has been investigated in a large number of numerical models. In coupled models the North Atlantic heat transport has been shown to be anticorrelated with the volume of sea ice in the Arctic Ocean (Docquier et al. 2019). Årthun and Eldevik (2016) analyzed a 500-yr-long simulation of the low-resolution coupled Bergen Climate Model and found that the heat entering the Norwegian Sea was a source of predictability for the Arctic temperature with a time lag of 14 years. More recently, Muilwijk et al. (2018) analyzed the variability in a century-long forced simulation of the same model. de Boer et al. (2018) studied the variability of volume transports through the Arctic straits and their correlations using both a 1/3° and a 1/12° coupled model similar to GC3. The ongoing HighResMip experiments (Roberts et al. 2019) will provide new opportunities to investigate the multidecadal variability of the AW inflow into the Arctic. Here, we use the relatively short GC3 experiment to document the interannual variability. We focus on the east–west exchanges within the Nordic seas, because they are expected to contribute to the variability of the pathways into the Arctic, and they are poorly documented.

We have computed time series of the annual mean volume and heat transports mapped in Figs. 7 and 10 and found no large trends in the 30-yr series (selected time series are shown in Figs. 11–13). Standard deviations based on annual means (std) are within the range of the CORE-II models (Ilicak et al. 2016) for the main pathways into the Arctic. For example, in the Barents Sea Opening (BSO) the std of volume transport in GC3 is 0.34 Sv (0.32–0.65 for the CORE-II models) and the std of heat transport is 10.2 TW (5.6–13.6 in CORE-II). Correlations between sections are presented in Table 3; unless indicated, all correlations reported in this paper are significant at the 95% level ($p$ value $< 0.05$).

In Fram Strait, there is a strong anticorrelation (−0.9) between the southward EGC branch along Greenland (Fram W) and the northward Spitzbergen Current branch along Svalbard (Fram E), an anticorrelation that was also found in a different model by Muilwijk et al. (2018). The std of volume transport is thus larger for each individual branch (0.81 and 0.87 Sv) than for the total flow through Fram Strait [0.45 Sv, consistent with Schauer et al. (2008)]. Interestingly, the heat transports of the two branches are also anticorrelated, but less strongly so than their volume transports (−0.4). This anticorrelation may be due to a recirculation of AW north of 79°N. As expected, the variability of the total heat transport through Fram Strait is dominated by the eastern branch carrying warm AW (correlation of 0.96). The std of the total heat transport through Fram Strait, 10.6 TW, is larger than the one found in the CORE-II models, reflecting the stronger and more realistic exchange flow in GC3 compared with lower-resolution models. At the southern entrance of the Nordic seas, the volume transports on both sides of Iceland are strongly anticorrelated (−0.7 between the Denmark and Icl-Norw sections; Table 3). This is expected, because both these transports are affected by the same atmospheric variability (Sorterberg et al. 2005), but it does not result in a similar correlation for the heat transport through these sections. There is also a correlation between the volume transport at the entrance of the Nordic seas and Fram Strait, as suggested by de Boer et al. (2018).

We focus now on the east–west exchanges. First, we consider the interannual variability of the recirculation over Knipovich Ridge, compared with the branches that exit the Norwegian Sea through Fram Strait and the BSO (Fig. 11). As expected, there is a correlation (0.5) between the volume transport exiting through Fram Strait (Fram E) and the volume flowing westward over Knipovich Ridge. In absolute values this is an anticorrelation: when more volume follows the Spitzbergen Current, less recirculates south of Fram Strait, and vice versa. However this relationship does not hold for the transport of heat. The heat transports across the Fram East section and across Knipovich Ridge tend to covary, indicating a stronger

TABLE 3. Correlations between volume transports and heat transports across sections pairs, computed from 30 years of annual means in the GC3 model. In this table, all transports are counted positive eastward and northward. Correlations below 95% confidence index ($p$ value higher than 0.05) are not shown. The sections follow the pathways indicated in Fig. 7. The western, eastern, and full sections are indicated for Fram Strait. BSO is the Barents Sea Opening; Knip and Mohn are the sections across Knipovich and Mohn Ridges. Integrated transports between the island of Jan Mayen and Iceland and Greenland (Jmay-Icl and Jmay-Gre) are indicated, as well as transports through Denmark Strait and between Iceland and Norway (denoted Denmark and Icl-Norw, respectively).

| | Fram W | Fram E | Fram | BSO | Knip | Mohn | Jmay-Icl | Jmay-Gre | Denmark | Icl-Norw |
|---|---|---|---|---|---|---|---|---|---|---|
| Volume | | | | | | | | | | |
| Fram W | 1.0 | — | — | — | — | — | — | — | — | — |
| Fram E | −0.9 | 1.0 | — | — | — | — | — | — | — | — |
| Fram | 0.4 | | 1.0 | — | — | — | — | — | — | — |
| BSO | | | −0.4 | 1.0 | — | — | — | — | — | — |
| Knip | −0.6 | 0.5 | −0.4 | | 1.0 | — | — | — | — | — |
| Mohn | −0.5 | | −0.5 | | | 1.0 | — | — | — | — |
| Jmay-Icl | | | | | | −0.6 | 1.0 | — | — | — |
| Jmay-Gre | 0.4 | −0.6 | | | | 0.4 | −0.7 | 1.0 | — | — |
| Denmark | | −0.4 | | | | −0.4 | 0.4 | | 1.0 | — |
| Icl-Norw | | 0.4 | 0.5 | | | | | −0.6 | −0.7 | 1.0 |
| Heat | | | | | | | | | | |
| Fram W | 1.0 | — | — | — | — | — | — | — | — | — |
| Fram E | −0.4 | 1.0 | — | — | — | — | — | — | — | — |
| Fram | | 1.0 | 1.0 | — | — | — | — | — | — | — |
| BSO | | 0.4 | 0.4 | 1.0 | — | — | — | — | — | — |
| Knip | | | | | 1.0 | — | — | — | — | — |
| Mohn | | −0.4 | −0.4 | | | 1.0 | — | — | — | — |
| Jmay-Icl | | | | 0.4 | | | 1.0 | — | — | — |
| Jmay-Gre | | | | | 0.6 | | −0.5 | 1.0 | — | — |
| Denmark | | | | | | | 0.7 | | 1.0 | — |
| Icl-Norw | | 0.7 | 0.6 | 0.6 | | −0.5 | | | | 1.0 |

influence of temperature variability than volume transport. Note, however, that the positive correlation of heat transports suggested by Fig. 11 is not significant. There is also no significant correlation between the volume transport exiting through BSO and the Fram East section, contrary to Muilwijk et al. (2018), who found a high correlation in their low-resolution model. One possible explanation is the presence of eddies in GC3, which may contribute to decorrelate the transports at the interannual time scale. This is in agreement with de Boer et al. (2018), who found a correlation of −0.9 between the total Fram and BSO transports in a low-resolution model, but only −0.5 in the high-resolution case; and also with Asbjørnsen et al.'s (2019) conclusion that eddy parameterizations have a dampening effect on interannual variability of heat fluxes. The correlation is similar in CG3 (−0.4; see Table 3). Unlike the volume transports, the heat transports through Fram East and BSO are correlated positively at lag zero (0.4), indicating that temperature anomalies can affect both sections the same year.

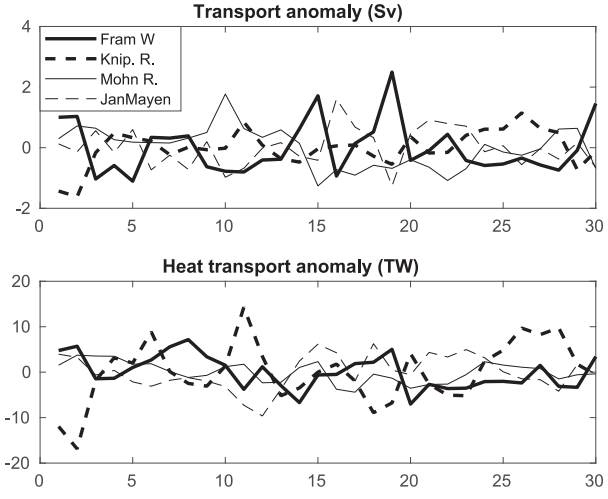


FIG. 12. Interannual anomalies of volume and heat transport across the four sections enclosing the Greenland Sea: the western part of Fram Strait (Fram W), flow over Knipovich Ridge (Knip. R) and Mohn Ridge (Mohn R.), and between Greenland and the island of Jan Mayen. The time axis is in model years.

The variability of the four inflows and outflows of the Greenland Sea is represented in Fig. 12. The std of the heat flux over Knipovich Ridge (6.7 TW) is about twice as large as the three other sections. In constrast, for the volume flux the EGC (Fram W section) is the branch with the largest variability. The volume flux entering over Knipovich Ridge and exiting over Mohn Ridge are similar (1.8 and 2.1 Sv), as well as their standard deviations (0.59 and 0.66 Sv), but these two branches are not connected by a simple loop. Indeed, the Mohn Ridge volume flux is not correlated with the Knipovich Ridge flux at the interannual time scale, while it has significant correlations with the Fram West and Jan Mayen-Greenland transports (0.5 and 0.4, respectively, Table 3). The absence of correlation between the circulations over Knipovich and Mohn Ridges is consistent

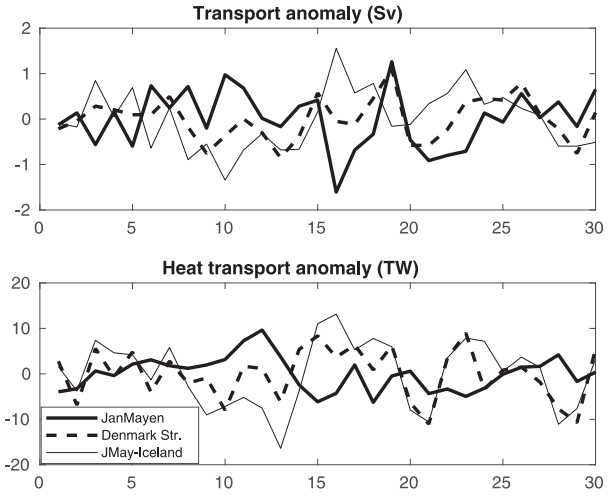


FIG. 13. Interannual anomalies of volume and heat transport across the sections enclosing the Iceland Sea: Denmark Strait, flow between Greenland and Jan Mayen (JanMayen), and flow between Jan Mayen and Iceland (JMay-Iceland). The time axis is in model years.

with Håvik et al. (2017), who observed that a significant part of the warm water carried by the recirculation south of Fram Strait enters the EGC and can then be entrained into the Greenland gyre circulation or carried along the Greenland slope into the Iceland Sea. The heat transports in GC3 are consistent with the circulation pattern observed by Håvik et al. (2017), with a strong correlation (0.6) between the heat transport anomalies over Knipovich Ridge and across the Jan Mayen–Greenland section (appearing as an anticorrelation in Fig. 12 because of the sign convention).

Let us finally consider the Iceland Sea (Fig. 13). The EGC inflow between Jan Mayen island and Greenland does not show any significant correlation with the Denmark Strait section. On the other hand, the transport between Jan Mayen and Iceland is correlated with both the EGC and Denmark Strait transports. For volume transport the correlation is strongest with the Jan Mayen–Greenland branch (−0.7) than with the Denmark Strait branch (0.4); for heat transport, the opposite is true and there is a strong correlation between heat transport anomalies through Denmark Strait and between Jan Mayen and Iceland (0.7), probably due to the variability of the East Icelandic Current, which connects these two sections. Finally, eastward transports north and south of Jan Mayen are anticorrelated (−0.6 correlation between Mohn and Jmay-Icl; Table 3): a strong transport over Mohn Ridge means less transport south of Jan Mayen and vice versa. However, despite this relationship between volume transports, there is no correlation of the heat transports carried by these two branches at interannual time scales.

In summary, the 30-yr time series of transports between the Norwegian Sea and the Greenland–Iceland Seas shows that the variability of east–west transports at interannual time scales is comparable to the variability of the exchanges with the Atlantic or the Arctic. Two branches play a key role by carrying relatively warm waters of Atlantic origin between the eastern and western basins: the recirculation over Knipovich Ridge south of Fram Strait, and the East Icelandic Current. The coupled model suggests that the variability of the Knipovich branch drives part of the variability of the EGC heat transport between Greenland and the island of Jan Mayen.

## 6. Conclusions

In this study we have used a global, fully coupled atmosphere–land–ocean–sea ice model to investigate the regional dynamics of the Nordic seas. This is made possible by the high resolution of the GC3 simulation, which has been found to improve a number of key ocean circulation processes (Hewitt et al. 2016, 2017). For example, de Boer et al. (2018) noted that the 1/12° model had a more realistic transport through the Canadian Archipelago than a lower-resolution climate model. In the Nordic seas, the integrated sea ice area is much closer to observations in GC3 than in the three coupled climate models investigated by Langehaug et al. (2017). Additionally the heat transport into the Nordic seas is very well represented, compared with the climate models evaluated by Heuzé and Årthun (2019). For regional analyses such as ours, model simulations forced by a prescribed atmospheric state are often preferred to fully coupled models; recent exemples at high resolution are Aksenov et al. (2010), Wekerle et al. (2017), Schlichtholz et al. (2019), and Ypma et al. (2019). Before choosing the CG3 coupled simulation, we compared it with a simulation of the same 1/12° ice–ocean model forced by CORE atmospheric forcings, and found that biases were similar in both the coupled and the forced simulations (not shown). We found that the forced model overestimates the ice concentration (similar to Fig. 2) and displays SST biases (similar to Fig. 4). For our investigation of the heat balance we have chosen the coupled model because it has fully consistent ocean–ice–atmosphere fluxes, contrary to forced models that may have spurious fluxes where the simulated ice distribution does not match the observed one (Griffies et al. 2009).

We have taken advantage of the high resolution of the model (4.7 km) to compute a full-depth heat budget separately for different subregions of the Nordic seas. By considering the ocean heat budget under the sea ice, we highlight the importance of cooling due to ice melt in the Greenland and Iceland seas. This cooling is concentrated along the path of the EGC as well as west of Svalbard. The model conserves mass and does not have any large drift of its heat content, a necessary condition to compute full-depth volume and heat budgets in the subregions. These integrated budgets, in three separate ocean basins, are the main result of this paper (Figs. 7 and 10). Contrary to Segtnan et al. (2011), we do not find that a net east–west heat exchange between the Norwegian Sea and the Greenland–Iceland Seas is necessary to close the budget. The east–west exchange of heat in the model is dominated by the recirculation over Knipovich Ridge to the north, exporting heat out of the Norwegian Sea, and the East Icelandic Current to the south, bringing heat into the Norwegian Sea. In the GC3 model these heat transports almost cancel each other. The main discrepancy between Segtnan's estimate and ours is the heat transport through Denmark Strait, which Segtnan

assumes to be 5 TW to the south for liquid water. Such a southward heat transport does not seem compatible with the inflow of Atlantic Water along the Icelandic slope, which carries 22–24 TW northward (Østerhus et al. 2005; Chafik and Rossby 2019). We thus consider that the heat convergence of 46 TW in the Greenland–Iceland Seas in GC3 is more realistic than Segtnan's 9 TW.

We have estimated, for the first time, the eddy contribution to the time-mean heat transports in the Nordic seas. Eddy transports play an important role in the coupled simulation. The eddy heat fluxes represent a quarter of the total heat convergence into the Greenland–Iceland Seas. Eddy fluxes are important over Knipovich Ridge (4.1 TW), over the Iceland–Faroe Ridge (8.1 TW), through Denmark Strait (7.7 TW), and in the Barents Sea opening (5.9 TW). Theses values may be underestimated, as suggested by the comparison with drifters (Fig. 5), because of the model grid resolution, which is still insufficient to fully resolve eddies in weakly stratified regions where the Rossby radius is small (7 km in the Norwegian Sea; Nurser and Bacon 2014). These strong eddy heat fluxes have important implications for observational strategies to measure heat transports in the Nordic seas. The eddy-generated oceanic "intrinsic" variability impacts the interannual time scales (Penduff et al. 2018). Also, as eddies are generated locally, their variability may make it more difficult to find spatially coherent patterns of heat anomalies propagating from the Atlantic to the Arctic in high-resolution models, as compared to low-resolution climate models. Note that even in the absence of ocean eddies, coherent surface anomalies tend to be masked by the strong interannual variability of local surface fluxes (Asbjørnsen et al. 2019).

Despite its heat balance being as good as the one achieved in forced models in multidecadal simulations, the coupled model has some biases that may influence its performance for projections of future climate. The amount of heat entering the Nordic seas from the North Atlantic is probably overestimated by 10%–15%. The excess heat is not released to the atmosphere but rather enters the Arctic Ocean, where it could potentially affect the sea ice cover and trigger climate feedbacks. The heat loss may be underestimated in GC3 in the Norwegian Sea due to the weakness of the Norwegian Atlantic Front Current. Our findings are consistent with the general pattern of large heat transports in the Atlantic and into the Arctic at high resolution (Roberts et al. 2019). Docquier et al. (2019) also found that coupled models at a resolution of 1/4° tend to have a higher Atlantic heat transport and, consequently, a lower Arctic sea ice than coarser-resolution models. Such a dependency of the meridional heat transport in the Atlantic on ocean grid resolution is well known. It has been first demonstrated in ocean models forced by a prescribed atmosphere (e.g., Hecht and Smith 2008; Treguier et al. 2012). Forced ocean model experiments, such as defined by the Ocean Model Intercomparison Project (Griffies et al. 2016), will thus be useful to develop and validate future high-resolution coupled models for climate.

*Acknowledgments.* We thank Pascale L'Herminier for sharing her views of the circulation of the Nordic seas and drafting Figure 1. Anne Marie Treguier is supported by CNRS, and Camille Lique by Ifremer. Pierre Mathiot and Tim Graham are supported by the Met Office Hadley Centre Climate Programme funded by BEIS and Defra (GA01101). We acknowledge extensive use of the supercomputers at the Met Office and the ARCHER U.K. National Supercomputing Service to complete the simulations and the CEDA-JASMIN platform for enabling data storage and model analysis. The authors acknowledge the JWCRP Joint Marine Modelling Programme for providing support and access to model configurations and output.

*Data availability statement.* The GC3 model data are available via the CEDA-JASMIN platform, upon request to the MetOffice authors.

## REFERENCES

Aksenov, Y., S. Bacon, A. C. Coward, and A. G. Nurser, 2010: The North Atlantic inflow to the Arctic Ocean: High-resolution model study. *J. Mar. Syst.*, **79** (1–2), 1–22, https://doi.org/10.1016/j.jmarsys.2009.05.003.

Appen, W.-J., D. Mastropole, R. S. Pickart, H. Valdimarsson, S. Jónsson, and J. B. Girton, 2017: On the nature of the mesoscale variability in Denmark Strait. *J. Phys. Oceanogr.*, **47**, 567–582, https://doi.org/10.1175/JPO-D-16-0127.1.

Årthun, M., and T. Eldevik, 2016: On anomalous ocean heat transport toward the Arctic and associated climate predictability. *J. Climate*, **29**, 689–704, https://doi.org/10.1175/JCLI-D-15-0448.1.

Asbjørnsen, H., M. Arthun, O. Skagseth, and T. Eldevik, 2019: Mechanisms of ocean heat anomalies in the Norwegian Sea. *J. Geophys. Res. Oceans*, **124**, 2908–2923, https://doi.org/10.1029/2018JC014649.

Barnier, B., and Coauthors, 2006: Impact of partial steps and momentum advection schemes in a global ocean circulation model at eddy-permitting resolution. *Ocean Dyn.*, **56**, 543–567, https://doi.org/10.1007/s10236-006-0082-1.

Barton, B. I., Y.-D. Lenn, and C. Lique, 2018: Observed Atlantification of the Barents Sea causes the polar front to limit the expansion of winter sea ice. *J. Phys. Oceanogr.*, **48**, 1849–1866, https://doi.org/10.1175/JPO-D-18-0003.1.

Berx, B., B. Hansen, S. Østerhus, K. M. Larsen, T. Sherwin, and K. Jochumsen, 2013: Combining in situ measurements and altimetry to estimate volume, heat and salt transport variability through the Faroe-Shetland Channel. *Ocean Sci.*, **9**, 639–654, https://doi.org/10.5194/os-9-639-2013.

Beszczynska-Möller, A., E. Fahrbach, U. Schauer, and E. Hansen, 2012: Variability in Atlantic water temperature and transport at the entrance to the Arctic Ocean, 1997–2010. *ICES J. Mar. Sci.*, **69**, 852–863, https://doi.org/10.1093/icesjms/fss056.

Bourke, R. H., A. M. Weigel, and R. G. Paquette, 1988: The westward turning branch of the West Spitsbergen Current. *J. Geophys. Res. Oceans*, **93**, 14 065–14 077, https://doi.org/10.1029/JC093iC11p14065.

——, R. G. Paquette, and R. F. Blythe, 1992: The Jan Mayen Current of the Greenland Sea. *J. Geophys. Res. Oceans*, **97**, 7241–7250, https://doi.org/10.1029/92JC00150.

Broomé, S., L. Chafik, and J. Nilsson, 2020: Mechanisms of decadal changes in sea surface height and heat content in the eastern Nordic seas. *Ocean Sci.*, **16**, 715–728, https://doi.org/10.5194/os-16-715-2020.

Cavalieri, D. J., C. L. Parkinson, P. Gloersen, and H. J. Zwally, 1996: Sea ice concentrations from Nimbus-7 SMMR and DMSP SSM/

I-SSMIS Passive Microwave Data. NASA National Snow and Ice Data Center Distributed Active Archive Center, accessed 7 November 2018, https://doi.org/10.5067/8GQ8LZQVL0VL.

Chafik, L., and T. Rossby, 2019: Volume, heat, and freshwater divergences in the subpolar North Atlantic suggest the Nordic seas as key to the state of the meridional overturning circulation. *Geophys. Res. Lett.*, **46**, 4799–4808, https://doi.org/10.1029/2019GL082110.

Craig, A., S. Valcke, and L. Coquart, 2017: Development and performance of a new version of the OASIS coupler, OASIS3-MCT_3.0. *Geosci. Model Dev.*, **10**, 3297–3308, https://doi.org/10.5194/gmd-10-3297-2017.

de Boer, A. M., E. Gavilan Pascual-Ahuir, D. P. Stevens, L. Chafik, D. K. Hutchinson, Q. Zhang, L. C. Sime, and A. J. Willmott, 2018: Interconnectivity between volume transports through Arctic straits. *J. Geophys. Res. Oceans*, **123**, 8714–8729, https://doi.org/10.1029/2018JC014320.

Deshayes, J., R. Curry, and R. Msadek, 2014: CMIP5 model intercomparison of freshwater budget and circulation in the North Atlantic. *J. Climate*, **27**, 3298–3317, https://doi.org/10.1175/JCLI-D-12-00700.1.

de Steur, L., E. Hansen, C. Mauritzen, A. Beszczynska-Möller, and E. Fahrbach, 2014: Impact of recirculation on the East Greenland Current in Fram Strait: Results from moored current meter measurements between 1997 and 2009. *Deep-Sea Res. I*, **92**, 26–40, https://doi.org/10.1016/j.dsr.2014.05.018.

Dickson, R., J. Meincke, and P. Rhines, Eds., 2008: Arctic–subarctic ocean fluxes. *Defining the Role of the Northern Seas in Climate*, R. R. Dickson, J. Meincke, and P. Rhines, Eds., Springer, 1–13.

Docquier, D., and Coauthors, 2019: Impact of model resolution on Arctic sea ice and North Atlantic ocean heat transport. *Climate Dyn.*, **53**, 4989–5017, https://doi.org/10.1007/s00382-019-04840-y.

Dugstad, J., I. Fer, J. LaCasce, M. Sanchez de La Lama, and M. Trodahl, 2019: Lateral heat transport in the Lofoten Basin: Near-surface pathways and subsurface exchange. *J. Geophys. Res. Oceans*, **124**, 2992–3006, https://doi.org/10.1029/2018JC014774.

Gascard, J., and K. Mork, 2008: Climatic importance of large scale and mesoscale circulation in the Lofoten Basin deduced from Lagrangian observations. *Arctic–Subarctic Ocean Fluxes*, R. Dickson, J. Meincke, and P. Rhines, Eds., Springer, 131–144.

Germe, A., M.-N. Houssais, C. Herbaut, and C. Cassou, 2011: Greenland Sea sea ice variability over 1979–2007 and its link to the surface atmosphere. *J. Geophys. Res. Oceans*, **116**, C10034, https://doi.org/10.1029/2011JC006960.

Good, S. A., M. J. Martin, and N. A. Rayner, 2013: EN4: Quality controlled ocean temperature and salinity profiles and monthly objective analyses with uncertainty estimates. *J. Geophys. Res. Oceans*, **118**, 6704–6716, https://doi.org/10.1002/2013JC009067.

Griffies, S. M., and Coauthors, 2009: Coordinated Ocean-ice Reference Experiments (COREs). *Ocean Modell.*, **26** (1-2), 1–46, https://doi.org/10.1016/j.ocemod.2008.08.007.

——, and Coauthors, 2016: OMIP contribution to CMIP6: Experimental and diagnostic protocol for the physical component of the Ocean Model Intercomparison Project. *Geosci. Model Dev.*, **9**, 3231–3296, https://doi.org/10.5194/gmd-9-3231-2016.

Hansen, B., K. M. H. Larsen, H. Hátún, R. Kristiansen, E. Mortensen, and S. Østerhus, 2015: Transport of volume, heat, and salt towards the Arctic in the Faroe Current 1993–2013. *Ocean Sci.*, **11**, 743–757, https://doi.org/10.5194/os-11-743-2015.

Harden, B., and Coauthors, 2016: Upstream sources of the Denmark Strait overflow: Observations from a high-resolution mooring array. *Deep-Sea Res. I*, **112**, 94–112, https://doi.org/10.1016/j.dsr.2016.02.007.

Hattermann, T., P. E. Isachsen, W.-J. von Appen, J. Albretsen, and A. Sundfjord, 2016: Eddy-driven recirculation of Atlantic water in Fram Strait. *Geophys. Res. Lett.*, **43**, 3406–3414, https://doi.org/10.1002/2016GL068323.

Håvik, L., R. S. Pickart, K. Våge, D. Torres, A. M. Thurnherr, A. Beszczynska-Möller, W. Walczowski, and W.-J. von Appen, 2017: Evolution of the East Greenland Current from Fram Strait to Denmark Strait: Synoptic measurements from summer 2012. *J. Geophys. Res. Oceans*, **122**, 1974–1994, https://doi.org/10.1002/2016JC012228.

Hecht, M., and R. Smith, 2008: Towards a physical understanding of the North Atlantic: A review of model studies in an eddying regime. *Ocean Modeling in an Eddying Regime, Geophys. Monogr.*, Vol. 177, Amer. Geophys. Union, 213–240.

Heuzé, C., and M. Årthun, 2019: The Atlantic inflow across the Greenland–Scotland ridge in global climate models (CMIP5). *Elementa Sci. Anthropocene*, **7**, 16, https://doi.org/10.1525/elementa.354.

Hewitt, H. T., D. Copsey, I. D. Culverwell, C. M. Harris, R. S. R. Hill, A. B. Keen, A. J. McLaren, and E. C. Hunke, 2011: Design and implementation of the infrastructure of HadGEM3: The next-generation Met Office climate modelling system. *Geosci. Model Dev.*, **4**, 223–253, https://doi.org/10.5194/gmd-4-223-2011.

——, and Coauthors, 2016: The impact of resolving the Rossby radius at mid-latitudes in the ocean: Results from a high-resolution version of the Met Office GC2 coupled model. *Geosci. Model Dev.*, **9**, 3655–3670, https://doi.org/10.5194/gmd-9-3655-2016.

——, and Coauthors, 2017: Will high-resolution global ocean models benefit coupled predictions on short-range to climate time-scales? *Ocean Modell.*, **120**, 120–136, https://doi.org/10.1016/j.ocemod.2017.11.002.

Høydalsvik, F., C. Mauritzen, K. Orvik, J. LaCasce, C. Lee, and J. Gobat, 2013: Transport estimates of the western branch of the Norwegian Atlantic Current from glider surveys. *Deep-Sea Res. I*, **79**, 86–95, https://doi.org/10.1016/j.dsr.2013.05.005.

Hunke, E., W. Lipscomp, A. K. Turner, and N. Jeffery, and S. Elliott, 2015: CICE: The Los Alamos Sea Ice Model Documentation and Software User's Manual, version 5.1. Doc. LA-CC-06-012, 116 pp.

Ilicak, M., and Coauthors, 2016: An assessment of the Arctic Ocean in a suite of interannual CORE-II simulations. Part III: Hydrography and fluxes. *Ocean Modell.*, **100**, 141–161, https://doi.org/10.1016/j.ocemod.2016.02.004.

Isachsen, P. E., I. Koszalka, and J. H. LaCasce, 2012: Observed and modeled surface eddy heat fluxes in the eastern Nordic seas. *J. Geophys. Res.*, **117**, C08020, https://doi.org/10.1029/2012JC007935.

Jochumsen, K., D. Quadfasel, H. Valdimarsson, and S. Jónsson, 2012: Variability of the Denmark Strait overflow: Moored time series from 1996–2011. *J. Geophys. Res.*, **117**, C12003, https://doi.org/10.1029/2012JC008244.

Jónsson, S., 2007: Volume flux and fresh water transport associated with the East Icelandic Current. *Prog. Oceanogr.*, **73**, 231–241, https://doi.org/10.1016/j.pocean.2006.11.003.

——, and H. Valdimarsson, 2012: Water mass transport variability to the North Icelandic shelf, 1994–2010. *ICES J. Mar. Sci.*, **69**, 809–815, https://doi.org/10.1093/icesjms/fss024.

Langehaug, H. R., D. Matei, T. Eldevik, K. Lohmann, and Y. Gao, 2017: On model differences and skill in predicting sea surface temperature in the Nordic and Barents Seas. *Climate Dyn.*, **48**, 913–933, https://doi.org/10.1007/s00382-016-3118-3.

Laurindo, L. C., A. J. Mariano, and R. Lumpkin, 2017: An improved near-surface velocity climatology for the global ocean from drifter observations. *Deep-Sea Res. I*, **124**, 73–92, https://doi.org/10.1016/j.dsr.2017.04.009.

Liu, Y., P. H. Daum, H. Guo, and Y. Peng, 2008: Dispersion bias, dispersion effect, and the aerosol–cloud conundrum. *Environ. Res. Lett.*, **3**, 045021, https://doi.org/10.1088/1748-9326/3/4/045021.

Locarnini, R. A., and Coauthors, 2018: *Temperature*. Vol. 1, *World Ocean Atlas 2018*, NOAA Atlas NESDIS 81, 52 pp.

Lozier, M. S., and Coauthors, 2019: A sea change in our view of overturning in the subpolar North Atlantic. *Science*, **363**, 516–521, https://doi.org/10.1126/science.aau6592.

Marnela, M., B. Rudels, I. Goszczko, A. Beszczynska-Möller, and U. Schauer, 2016: Fram Strait and Greenland Sea transports, water masses, and water mass transformations 1999–2010 (and beyond). *J. Geophys. Res. Oceans*, **121**, 2314–2346, https://doi.org/10.1002/2015JC011312.

Moat, B. I., S. A. Josey, and B. Sinha, 2014: Impact of Barents Sea winter air–sea exchanges on Fram Strait dense water transport. *J. Geophys. Res. Oceans*, **119**, 1009–1021, https://doi.org/10.1002/2013JC009220.

Mork, K. A., and Ø. Skagseth, 2010: A quantitative description of the Norwegian Atlantic Current by combining altimetry and hydrography. *Ocean Sci.*, **6**, 901–911, https://doi.org/10.5194/os-6-901-2010.

——, ——, and H. Søiland, 2019: Recent warming and freshening of the Norwegian Sea observed by Argo data. *J. Climate*, **32**, 3695–3705, https://doi.org/10.1175/JCLI-D-18-0591.1.

Muilwijk, M., L. H. Smedsrud, M. Ilicak, and H. Drange, 2018: Atlantic water heat transport variability in the 20th century Arctic Ocean from a global ocean model and observations. *J. Geophys. Res. Oceans*, **123**, 8159–8179, https://doi.org/10.1029/2018JC014327.

Nurser, A. J. G., and S. Bacon, 2014: The Rossby radius in the Arctic Ocean. *Ocean Sci.*, **10**, 967–975, https://doi.org/10.5194/os-10-967-2014.

Orvik, K. A., Ø. Skagseth, and M. Mork, 2001: Atlantic inflow to the Nordic seas: Current structure and volume fluxes from moored current meters, VM-ADCP and SeaSoar-CTD observations, 1995–1999. *Deep-Sea Res. I*, **48**, 937–957, https://doi.org/10.1016/S0967-0637(00)00038-8.

Østerhus, S., W. R. Turrell, S. Jonsson, and B. Hansen, 2005: Measured volume, heat, and salt fluxes from the Atlantic to the Arctic Mediterranean. *Geophys. Res. Lett.*, **32**, L07603, https://doi.org/10.1029/2004GL022188.

——, and Coauthors, 2019: Arctic Mediterranean exchanges: A consistent volume budget and trends in transports from two decades of observations. *Ocean Sci.*, **15**, 379–399, https://doi.org/10.5194/os-15-379-2019.

Penduff, T., and Coauthors, 2018: Chaotic variability of ocean heat content: Climate-relevant features and observational implications. *Oceanography*, **31**, 63–71, https://doi.org/10.5670/oceanog.2018.210.

Polyakov, I. V., and Coauthors, 2017: Greater role for Atlantic inflows on sea-ice loss in the Eurasian basin of the Arctic Ocean. *Science*, **356**, 285–291, https://doi.org/10.1126/science.aai8204.

Quadfasel, D., and R. Käse, 2007: Present-day manifestation of the Nordic seas overflows. *Ocean Circulation: Mechanisms and Impacts—Past and Future Changes of Meridional Overturning*, *Geophys. Monogr.*, Vol. 173, Amer. Geophys. Union, 75–90, https://doi.org/10.1029/173GM07.

Reynolds, R. W., T. Smith, C. Liu, D. Chelton, K. Casey, and M. Schlax, 2007: Daily high-resolution-blended analyses for sea surface temperature. *J. Climate*, **20**, 5473–5496, https://doi.org/10.1175/2007JCLI1824.1.

Ricker, R., F. Girard-Ardhuin, T. Krumpen, and C. Lique, 2018: Satellite-derived sea ice export and its impact on Arctic ice mass balance. *Cryosphere*, **12**, 3017–3032, https://doi.org/10.5194/tc-12-3017-2018.

Ridley, J. K., E. W. Blockley, A. B. Keen, J. G. L. Rae, A. E. West, and D. Schroeder, 2018: The sea ice model component of HadGEM3-GC3.1. *Geosci. Model Dev.*, **11**, 713–723, https://doi.org/10.5194/gmd-11-713-2018.

Roberts, M. J., and Coauthors, 2019: Description of the resolution hierarchy of the global coupled HadGEM3-GC3.1 model as used in CMIP6 HighResMIP experiments. *Geosci. Model Dev.*, **12**, 4999–5028, https://doi.org/10.5194/gmd-12-4999-2019.

Rossby, T., C. Flagg, L. Chafik, B. Harden, and H. Søiland, 2018: A direct estimate of volume, heat, and freshwater exchange across the Greenland-Iceland-Faroe-Scotland ridge. *J. Geophys. Res. Oceans*, **123**, 7139–7153, https://doi.org/10.1029/2018JC014250.

Schauer, U., A. Beszczynska-Möller, W. Walczowski, E. Fahrbach, J. Piechura, and E. Hansen, 2008: Variation of measured heat flow through the Fram Strait between 1997 and 2006. *Arctic–Subarctic Ocean Fluxes*, R. Dickson, J. Meincke, and P. Rhines, Eds., Springer, 65–85.

Schlichtholz, P., J. Marciniak, and W. Maslowski, 2019: Proxies for heat fluxes to the Arctic Ocean through Fram Strait. *Ocean Modell.*, **137**, 21–39, https://doi.org/10.1016/j.ocemod.2019.02.007.

Segtnan, O. H., T. Furevik, and A. D. Jenkins, 2011: Heat and freshwater budgets of the Nordic seas computed from atmospheric reanalysis and ocean observations. *J. Geophys. Res.*, **116**, C11003, https://doi.org/10.1029/2011JC006939.

Sherwin, T., S. Hughes, W. Turrell, B. Hansen, and S. Østerhus, 2008: Wind-driven monthly variations in transport and the flow field in the Faroe-Shetland Channel. *Polar Res.*, **27**, 7–22, https://doi.org/10.1111/j.1751-8369.2007.00036.x.

Smedsrud, L. H., R. Ingvaldsen, J. E. Ø. Nilsen, and Ø. Skagseth, 2010: Heat in the Barents Sea: Transport, storage, and surface fluxes. *Ocean Sci.*, **6**, 219–234, https://doi.org/10.5194/os-6-219-2010.

——, and Coauthors, 2013: The role of the Barents Sea in the Arctic climate system. *Rev. Geophys.*, **51**, 415–449, https://doi.org/10.1002/rog.20017.

Søiland, H., L. Chafik, and T. Rossby, 2016: On the long-term stability of the Lofoten Basin eddy. *J. Geophys. Res. Oceans*, **121**, 4438–4449, https://doi.org/10.1002/2016JC011726.

Sorterberg, A., N. G. Kvamstø, and O. Byrkjedal, 2005: Wintertime Nordic seas cyclone variability and its impact on oceanic volume transports into the Nordic seas. *The Nordic Seas: An Integrated Perspective*, *Geophys. Monogr.*, Vol. 158, Amer. Geophys. Union, 137–156.

Storkey, D., and Coauthors, 2018: UK Global Ocean GO6 and GO7: A traceable hierarchy of model resolutions. *Geosci. Model Dev.*, **11**, 3187–3213, https://doi.org/10.5194/gmd-11-3187-2018.

Taburet, G., A. Sanchez-Roman, M. Ballarotta, M.-I. Pujol, J.-F. Legeais, F. Fournier, Y. Faugere, and G. Dibarboure, 2019: DUACS DT2018: 25 years of reprocessed sea level altimetry products. *Ocean Sci.*, **15**, 1207–1224, https://doi.org/10.5194/os-15-1207-2019.

Treguier, A. M., J. Deshayes, C. Lique, R. Dussin, and J. M. Molines, 2012: Eddy contributions to the meridional transport of salt in the North Atlantic. *J. Geophys. Res.*, **117**, C05010, https://doi.org/10.1029/2012JC007927.

Trodahl, M., and P. E. Isachsen, 2018: Topographic influence on baroclinic instability and the mesoscale eddy field in the northern North Atlantic Ocean and the Nordic seas. *J. Phys Oceanogr.*, **48**, 2593–2607, https://doi.org/10.1175/JPO-D-17-0220.1.

Tsubouchi, T., and Coauthors, 2012: The Arctic Ocean in summer: A quasi-synoptic inverse estimate of boundary fluxes and water mass transformation. *J. Geophys. Res.*, **117**, C01024, https://doi.org/10.1029/2011JC007174.

Våge, K., L. Papritz, L. Håvik, M. A. Spall, and G. W. K. Moore, 2018: Ocean convection linked to the recent ice edge retreat along east Greenland. *Nat. Commun.*, **9**, 1287, https://doi.org/10.1038/s41467-018-03468-6.

van der Linden, E. C., D. Le Bars, R. Bintanja, and W. Hazeleger, 2019: Oceanic heat transport into the Arctic under high and low $CO_2$ forcing. *Climate Dyn.*, **53**, 4763–4780, https://doi.org/10.1007/s00382-019-04824-y.

Walters, D., and Coauthors, 2019: The Met Office Unified Model Global Atmosphere 7.0/7.1 and JULES Global Land 7.0 configurations. *Geosci. Model Dev.*, **12**, 1909–1963, https://doi.org/10.5194/gmd-12-1909-2019.

Wekerle, C., Q. Wang, W.-J. von Appen, S. Danilov, V. Schourup-Kristensen, and T. Jung, 2017: Eddy-resolving simulation of the Atlantic water circulation in the Fram Strait with focus on the seasonal cycle. *J. Geophys. Res. Oceans*, **122**, 8385–8405, https://doi.org/10.1002/2017JC012974.

Williams, K. D., and Coauthors, 2018: The Met Office Global Coupled model 3.0 and 3.1 (GC3.0 and GC3.1) configurations. *J. Adv. Model. Earth Syst.*, **10**, 357–380, https://doi.org/10.1002/2017MS001115.

Ypma, S., N. Brüggemann, S. Georgiou, P. Spence, H. Dijkstra, J. Pietrzak, and C. Katsman, 2019: Pathways and watermass transformation of Atlantic water entering the Nordic seas through Denmark Strait in two high resolution ocean models. *Deep-Sea Res. I*, **145**, 59–72, https://doi.org/10.1016/j.dsr.2019.02.002.